Astrodynamics Vol. 7, No. 1, 31–50, 2023 https://doi.org/10.1007/s42064-022-0131-7

Geophysical and orbital environments of asteroid 469219 2016 HO3

Xiangyu Li[1,2], Daniel J. Scheeres[2], Dong Qiao[1](✉), and Zixuan Liu[1]

1. *School of Aerospace Engineering, Beijing Institute of Technology, Beijing 100081, China*
2. *Ann and H. J. Smead Aerospace Engineering Department, University of Colorado Boulder, 429 UCB, Boulder, CO 80309, USA*

ABSTRACT

Asteroid 469219 Kamo'oalewa, also named 2016 HO3, is a small-size fast-rotating near-Earth asteroid, which is a potential target for future explorations. Owing to its weak gravity and fast spin rate, the dynamics on the surface or in the vicinity of 2016 HO3 are significantly different from those of planets or other small bodies explored in previous missions. In this study, the geophysical and orbital environments of 2016 HO3 were investigated to facilitate a potential mission design. First, the geometric and geopotential topographies of 2016 HO3 were examined using different shape models. The lift-off and escape conditions on its fast-rotating surface were investigated. Then, the periodic orbits around 2016 HO3 were studied in the asteroid-fixed frame and the Sun–asteroid frame considering the solar radiation pressure. The stable regions of the terminator orbits were discussed using different parameters. Finally, the influence of the nonspherical shape on the terminator orbits was examined. The precise terminator orbits around a real shape model of 2016 HO3 were obtained and verified in the high-fidelity model. This study shows that the polar region of 2016 HO3 is the primary region for landing or sampling, and the terminator orbits are well suited for global mapping and measurements of 2016 HO3. The analysis and methods can also serve as references for the exploration of other small fast-rotating bodies.

KEYWORDS

asteroid 2016 HO3
geophysical environment
solar radiation pressure
terminator orbit

Research Article

Received: 8 October 2021
Accepted: 8 January 2022

1 Introduction

Solar system small bodies such as asteroids and comets have attracted scientific study for a long time as they may contain clues to understand the evolution of the solar system, the formation of planets, and the origin of life. Several missions to small bodies have been successfully performed in the past few years, and they have obtained abundant information about the composition and structure of these targets [1–7]. The targets in previous missions included near-Earth asteroids (NEAs) and main-belt asteroids with different spectral types as well as comets. The size of the targets has varied from hundreds of meters to hundreds of kilometers, and the rotation period has ranged from less than 1 h to more than 10 h. Meanwhile, more missions to metal asteroids [8], Trojan asteroids [9], and binary asteroids [10] are in progress, which will increase our knowledge of these asteroid types.

With the development of observational techniques, numerous small-sized asteroids (diameter of less than 100 m) have been found in recent years [11]. Some have a short rotation period, below "the rotation barrier" (less than 2 h) [12]. These features differentiate them from other small bodies studied in previous missions. The composition, formation, and dynamic evolution of such small fast-rotating bodies are still unknown, which makes them interesting targets for exploration. NEA 469219 Kamo'oalewa, or 2016 HO3, is one of such small bodies. It is also a quasi-satellite of the Earth [13], which has nearly the same orbital period as the Earth and remains stable in the neighborhood of the Earth–Moon system for a long time. Therefore, it is an easily accessible target with

✉ qiaodong@bit.edu.cn

frequent launch opportunities (approximately every half a year). Therefore, asteroid 2016 HO3 has been identified as a destination for several mission proposals [14]. In particular, the Chinese Space Agency issued its sample return mission to 2016 HO3 to determine its physical properties, chemical and mineral components, isotope composition, and structure.

The geophysical and orbital environments of an asteroid are crucial for mission planning. Extensive research has been conducted in this field. The distribution and evolution of the equilibrium points around irregularly shaped small bodies have been discussed [15–18]. The stability of orbits around small bodies has been investigated based on different gravitation field models [19, 20]. Periodic orbits under the combined influence of solar tides, solar radiation pressure (SRP), and nonspherical perturbation have been designed [21–26]. Meanwhile, the evolution of surface particles has been analyzed [27–29]. Van wal *et al.* [30] calculated the lift-off and escape velocities from the surface. Wen *et al.* [31] defined the surface-hopping domain. Li *et al.* [32] further discussed the influence of rough surfaces on landing motion by constructing rocky terrains generated based on the polyhedral model. These studies help us better understand the motions around small bodies. Before the OSIRIS-Rex mission, the detailed surface and interior states of Bennu were investigated [33] to prepare the mission plan. However, owing to its small size and fast spin rate, the dynamic environment on the surface or in the vicinity of 2016 HO3 might be different from that of other explored small bodies. The weak gravity cannot bind materials in low latitude regions [34]. The SRP is also non-negligible when we discuss orbital motions around 2016 HO3. It is therefore necessary to investigate the geophysical and orbital environments of asteroid 2016 HO3 prior to exploration missions. The aim of this study is to provide a detailed analysis of the possible surface and orbital motion on/around 2016 HO3 to facilitate the mission design. The main contributions of this study are as follows.

First, the geometric and geopotential topographies of asteroid 2016 HO3 were studied. The lift-off and escape conditions on the fast-rotating surface were investigated. Owing to its fast spin rate, objects resting on the surface may lift off or even escape from 2016 HO3 if they are not bound. Therefore, we analyzed the required velocities on the surface to avoid lift-off or escape. The surfaces were classified based on the different conditions. The range and direction of the surface velocity in different regions were examined.

Second, the periodic orbits and their stabilities in the asteroid-fixed frame and the Sun–asteroid rotating frame were investigated considering the SRP. Because the physical parameters of 2016 HO3 are still very uncertain, the stable region of terminator orbits around 2016 HO3 was analyzed with different parameters.

Third, the influence of the nonspherical perturbation on terminator orbits was examined. Terminator orbits of small bodies are usually solved based on a point-mass model or a spherical model. Asteroid 2016 HO3 has an elongated shape, which causes large gravity perturbations when compared with a spherical model. The precise terminator orbits under the non-spherical perturbation of 2016 HO3 were solved, and the effect of pole orientation on the offsets of terminator orbits was investigated.

The analysis and methods used in this study provide preliminary results of the motions around asteroid 2016 HO3, which can be used for mission planning once an accurate shape model and the physical parameters of 2016 HO3 are available. They also serve as references for the exploration of other small-sized fast-rotating bodies with characteristics similar to those of 2016 HO3.

The remainder of this paper is organized as follows. Section 2 describes the parameters and models of asteroid 2016 HO3 used in this study. Section 3 describes the geophysical environment of 2016 HO3. The geometric and geopotential topographies of 2016 HO3 with models of different shapes are discussed. The lift-off and escape conditions on the surface are analyzed. Section 4 investigates the orbital motion in the asteroid-fixed frame. The periodic motions in the Sun–asteroid rotating frame are described in Section 5. The influence of the nonspherical perturbation on terminator orbits is examined. Finally, Section 6 concludes the paper.

2 Shape model of 2016 HO3

2.1 Basic dynamics

The shape model of asteroid 2016 HO3 in this study is given. This observation suggests that 2016 HO3 is an L-type (S-type) asteroid with a mean radius of 18 m [35] and a spin period of 0.467 ± 0.008 h. A precise shape model of 2016 HO3 is currently unavailable, but the light curve shows a large amplitude, indicating that 2016 HO3

might be an elongated small body [36]. The possible size ratios were discussed based on the triaxial shape model [34]. We selected two size ratios for our study. The first model S_1 had ratios of $b/c = 1$ and $b/a = 0.4786$, which is the superior limit ratio for b/a. The second model S_2 had ratios of $b/c = 1.4142$ and $b/a = 0.3036$, which corresponded to a much more elongated shape. Based on a mean radius of 18 m, the sizes of the two models were S_1 : 58.8 m × 28.2 m × 28.2 m and S_2 : 88.9 m × 27.2 m × 19.3 m. Meanwhile, to better reflect the influence of irregular shapes, both ellipsoid and real-shape models were used to analyze the geophysical environment of asteroid 2016 HO3. The shape model of asteroid 1998 KY26 was used [37]. It has a similar size and spin rate to those of 2016 HO3, but the asteroid is closer to a spherical body. Therefore, the shape model was stretched or compressed to satisfy the size ratio. The two shape models are shown in Fig. 1.

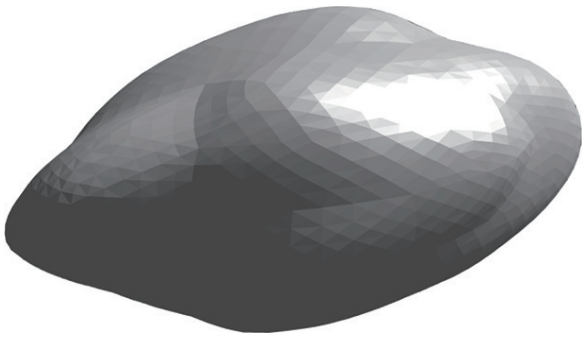

(a) Model S_1

(b) Model S_2

Fig. 1 Shape models of asteroid 2016 HO3 used in the study.

The ellipsoid integral and polyhedron methods were used to calculate the gravitational fields of the models. Here, we assume that 2016 HO3 has a constant density of $\rho = 2.5$ g/cm^3, which is a typical value of an S-type asteroid [38]. The spin rate is $\omega = 0.003737$ rad/s. An asteroid-fixed frame was established at the center of the mass. The X, Y, and Z axes were aligned with the maximum, medium, and minimum principal axes of inertia of the body, respectively. The spin axis was assumed to be along the Z axis. When we analyzed the geophysical environment of 2016 HO3, other perturbations, such as the SRP, electromagnetic force, and third-body gravity, were neglected. However, the effect of the SRP was considered when examining the orbital motions.

3 Geophysical environment of 2016 HO3

Based on the shape model and parameters presented above, the geophysical environment of asteroid 2016 HO3 was analyzed and mapped on the surface, including the geometric and geopotential topographies and their derivatives. The methods and definitions used in previous studies were applied. We modified the lift-off and escape velocities on the surface of a fast-spinning body.

3.1 Geometric and geopotential topography

First, the geometric topography of 2016 HO3 was examined, and it was used to describe the relative changes in the body's radius from the coordinate center and the orientation of the surface relative to the body-fixed frame. It is only related to the shape of an asteroid and is independent of the gravity and spin rate. The relative geometric altitudes and tilt angles of the two shape models are shown in Figs. 2 and 3, respectively. Here, the sea level or zero value was set as the lowest distance from the surface to the center. The tilt angle was defined as the angle between the surface normal vector and radius vector from the surface. It is evident that shape model S_2 has larger altitude and tilt angle. The relative altitudes were 17 m for S_1 and 36 m for S_2. Large tilt angles appeared near the end of the long axis, and small tilt angles were concentrated near the YZ plane. The maximum tilt

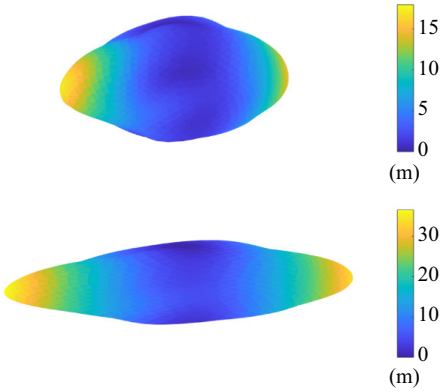

Fig. 2 Geometric altitude of two shape models.

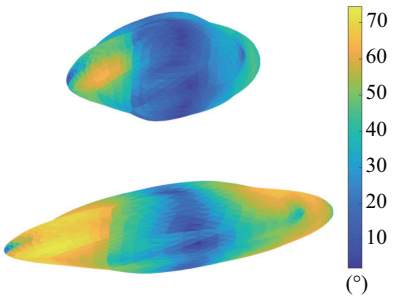

Fig. 3 Tilt angle of two shape models.

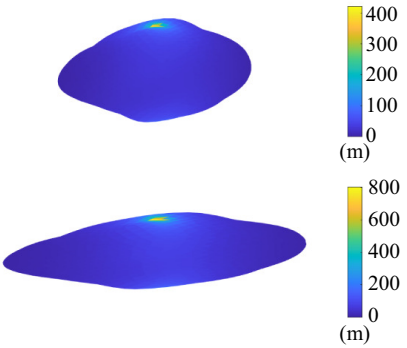

Fig. 4 Geopotential altitude of the two shape models.

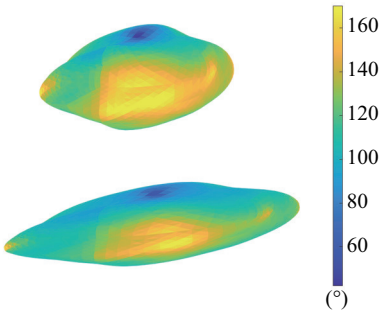

Fig. 5 Slope angle of the two shape models.

angle was 74° for S_2. The geometric topography varied according to the shape of the model. The tilt angles in the ellipsoid model had a similar distribution, but a smaller maximum value as the altitude near the two extremes changed smoothly. Another azimuthal angle can be defined within the tangential plane to determine the orientation of the surface in the body-fixed frame. Then, the orientation of the surface in the inertial frame can be solved, which is important for a landing mission, as the spacecraft needs to determine its attitude relative to the surface to maintain safety.

Compared with the geometric topography, the geopotential topography focuses on the relative changes in geopotential of a body and the orientation of the surface relative to surface acceleration. This is crucial to the characteristics of surface motion. Here, previous definitions of geopotential altitude and slope angle were used [33]. The surface slope was defined as the relative orientation between the surface normal vector and the local acceleration vector. The slope angle supplemented the angle between the surface normal and the total acceleration at the location. The lowest value of the geopotential across the surface was selected as the "sea level" [39]. Then, the geopotential value at a given location relative to the reference "sea level" was solved. The geopotential altitude at a given location was determined by dividing the relative geopotential value by the local total acceleration, which is in units of length. The geopotential altitude reflects the potential difference between two locations. Its value may be larger than the real geometric height or radius of the small body. Figures 4 and 5 show the results for the two models.

The geopotential topography of 2016 HO3 is different from the geometric topography because of the fast spin rate. The largest geopotential altitude of 2016 HO3 appears at the pole, but the "sea level" or the lowest geopotential altitude is located at the extremes of the major axis, which is opposite to the geometric altitude. The altitude changes sharply near the pole region. The maximum altitude is approximately 400 m in S_1 and increases to 800 m in S_2, indicating that the difference in energy across the surface is extremely large in an elongated fast-spinning body. The pole region is the only area where the slope angle is less than 90°, as shown in Fig. 5. In most areas, the surface has a large slope angle, indicating positive surface gravity. It requires cohesion or a grip force to maintain a particle or spacecraft on the surface. Owing to the uneven terrain, even the pole region may have a large slope angle. In our shape model, the minimum slope angle exceeded 40°. The ellipsoid models yielded similar results; however, the slope angle at the pole was reduced to 0. The geopotential altitude and slope angle are also related to the density of the small body. A higher density corresponds to lower altitude and smaller slope angle. These results imply that a fast spin rate significantly changes the surface environment of asteroids compared with planets or moons. Moreover, the elongated shape aggravates the disparity in energy over the surface.

The change in geopotential altitude can be associated with the amount of work required to move an object from one position to another, which is called the Jacobi

speed [33]. The relative Jacobi speed is the speed that a particle would gain when going from the highest point in the geopotential to a location, or the speed that a particle would require at a point to reach the highest point in the geopotential. The results for the relative Jacobi speeds in the two shape models are shown in Fig. 6. The difference in velocity is approximately 0.12 m/s for S_1 and increases to 0.18 m/s when the body has a longer major axis. However, it only provides the velocity from an energy perspective. This does not imply that the particle at the pole can move to the equator at a certain velocity. More factors should be considered, such as the lift-off and escape conditions.

3.2 Lift-off and sliding velocity

The applications of geopotential topography include the determination of lift-off and escape velocities. The lift-off velocity refers to the required tangential velocity on the surface to lift an object and is expressed as [30]:

$$V_{\rm l} = \pm\sqrt{\rho_{\rm l}^2(\hat{\boldsymbol{b}}_\delta\cdot\boldsymbol{\Omega})^2+\rho_{\rm l}\hat{\boldsymbol{b}}_{\rho_{\rm l}}\cdot\left[\boldsymbol{\Omega}\times(\boldsymbol{\Omega}\times\boldsymbol{R})-\frac{\partial U}{\partial\boldsymbol{R}}\right]}-\rho_{\rm l}\hat{\boldsymbol{b}}_\delta\cdot\boldsymbol{\Omega} \tag{1}$$

Here, $\boldsymbol{R}$ is the position vector of the initial point P and $\boldsymbol{\Omega}$ is the angular velocity of the asteroid $\boldsymbol{\Omega}=[0,0,\omega]^{\rm T}$. U is the gravity potential of the asteroid. $\rho_{\rm l}$ is the effective radius of curvature at point P. $\hat{\boldsymbol{b}}_{\rho_{\rm l}}$ is the unit vector from the center of curvature to point P, which is equal to the surface normal, $\hat{\boldsymbol{b}}_\delta=\hat{\boldsymbol{b}}_{\rho_{\rm l}}\times\hat{\boldsymbol{b}}_\theta$, where $\hat{\boldsymbol{b}}_\theta$ is an arbitrary unit vector on the tangential surface at P with azimuth η. Usually, there are two lift-off velocities along the directions $\hat{\boldsymbol{b}}_\theta$ and $-\hat{\boldsymbol{b}}_\theta$. The curvature radius $\rho_{\rm l}(\eta)$ changes with the azimuth η. Therefore, at each initial point P, we can determine the maximum and minimum lift-off velocities at two azimuth angles. Meanwhile, the lift-off velocity is significantly affected by $\rho_{\rm l}$. If applicable, the velocity will be extremely large at a local concave, and there will be a minimum radius of curvature if it is locally concave. Therefore, we were more interested in the lift-off velocity on convex surfaces. The ellipsoid models of asteroid 2016 HO3 were used first, as they are fully convex. The surface curvature of the ellipsoid was solved mathematically, and the principal curvatures and directions were determined. Subsequently, the curvature at any azimuth η was obtained to solve the corresponding lift-off velocity. Owing to the fast spin rate, the lift-off velocity on the surface of 2016 HO3 was significantly different from that on Bennu or 1999 KW4 alpha [40]. Figure 7 shows the maximum lift-off velocity in the latitude–longitude $\lambda-\phi$ map and the triaxial ellipsoid shape model. In the figures, the red points correspond to the initial positions. The length and direction of the black lines indicate the magnitude and direction of the maximum and minimum lift-off velocities at the initial position, respectively. As can be observed, the regions close to the extremes of the major axis are unsolvable. This means that there is no lift-off velocity or the lift-off velocity is zero. The object lifts off the surface, even if it is stationary. The directions of the maximum lift-off in the other areas are shown in Fig. 7(b). The minimum lift-off velocities and directions are shown in Fig. 8. It is interesting to note that, except for the polar region, the minimum lift-off velocity has the same direction as the maximum velocity. This implies that the minimum velocity was negative in these regions. An object requires a certain surface velocity to maintain

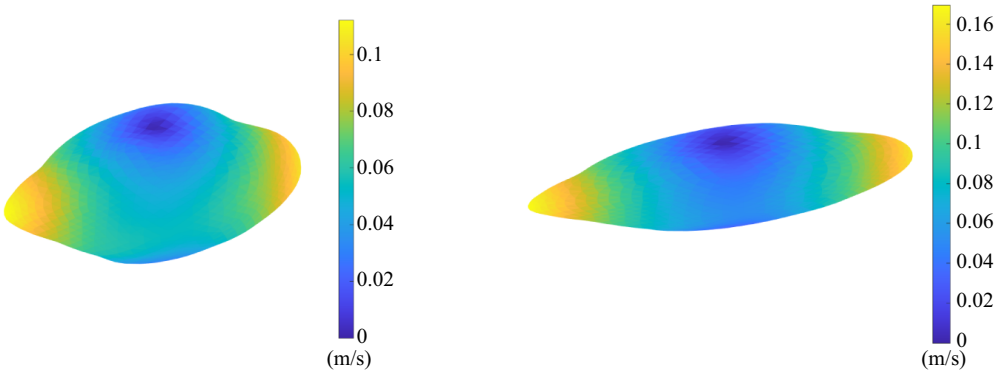

(a) Model S_1 (b) Model S_2

Fig. 6 Relative Jacobi speeds.

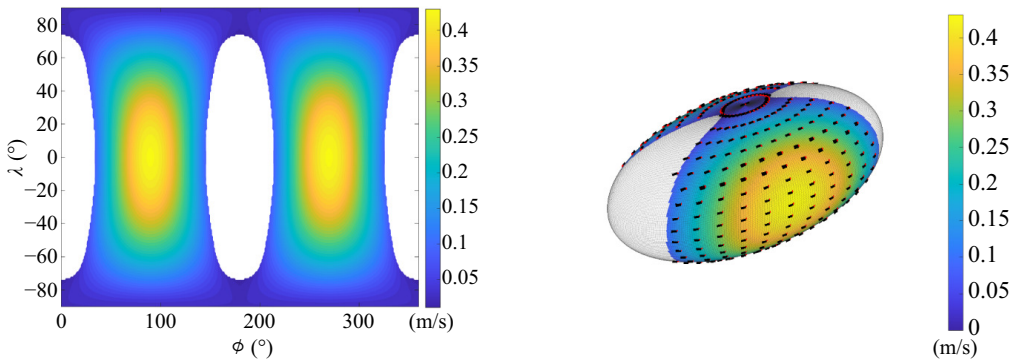

(a) Latitude–longitude $\lambda - \phi$ map (b) Triaxial ellipsoid shape model

Fig. 7 Magnitudes and directions of maximum lift-off/sliding velocity.

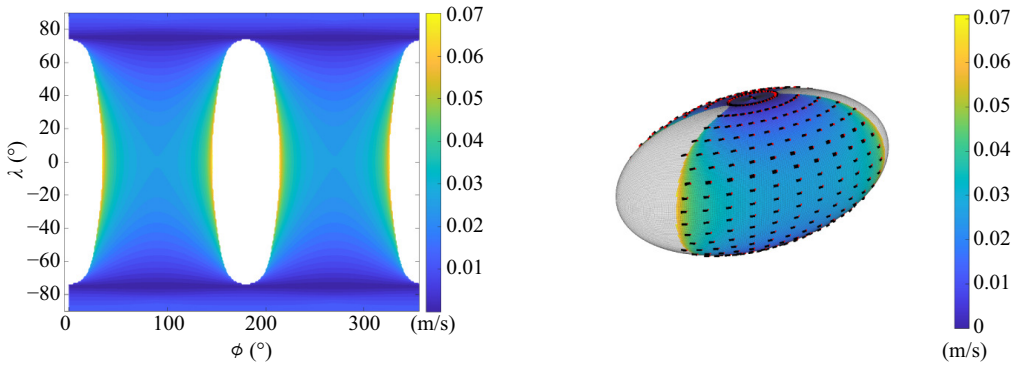

(a) Latitude–longitude $\lambda - \phi$ map (b) Triaxial ellipsoid shape model

Fig. 8 Magnitudes and directions of minimum lift-off/sliding velocity.

contact with the surface at the initial position. Otherwise, it will naturally be lifted off. In this case, we refer to the negative lift-off velocity as the sliding velocity. The sliding velocity has a constrained direction and value. Figure 9 shows the boundaries of the sliding velocities at different initial points. In the figure, the dashed red line from the stars to the ellipse indicates the maximum or minimum sliding/lift-off velocity in the given direction. If the star is inside the ellipse, the initial point has a lift-off velocity in any direction. An ellipse corresponds to the maximum value. Otherwise, the initial point had a sliding velocity in the constrained direction. The feasible sliding velocity vector falls inside the ellipse. This implies that the ellipse corresponds to both the maximum and minimum sliding velocities in a specific direction. The lift-off velocity was effective in any direction only near the polar region. Increasing the major axis will increase the minimum required sliding velocity, but it does not change significantly, as does the decrease in density.

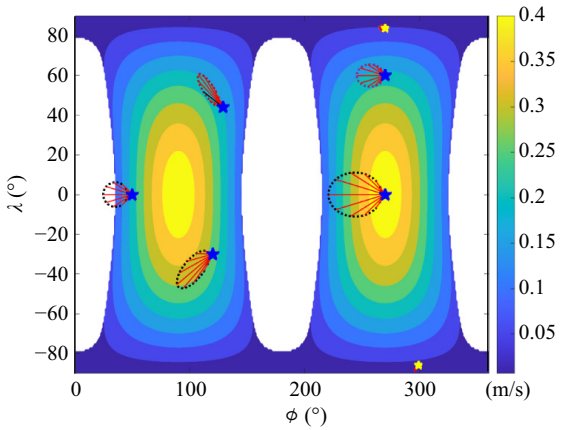

Fig. 9 Boundary of sliding/lift-off velocities at different locations. The sliding velocity is indicated by a blue star, and the initial point is outside the boundary. The lift-off velocity is shown as a yellow star, where the initial point is inside the boundary and the velocity in any direction can be found.

Two conclusions can be drawn from these results. First, if we want to land on the surface, then the polar region

is the only possible region to remain stationary. The tangential velocity of the spacecraft should be smaller than 0.01 m/s to avoid lifting off when it lands on the surface. Second, it is still possible to move on the surface of a fast-spinning asteroid if the surface velocity can be controlled within a certain range. However, owing to the existence of an infeasible region near the major axis, the surface motion might be temperate.

Then, the real shape model was applied, and the mean curvature at each vertex of the polyhedron model was solved. Some vertices are concave in one direction but convex in the other. This means that the maximum lift-off velocity is unbounded from above. Therefore, we only provided the minimum sliding velocity or lift-off velocity on the surface, as shown in Fig. 10. The types of regions are shown in Fig. 10(a). As shown, the local terrain may change the type of region. Some regions near the pole may require a surface velocity to avoid lifting, and the lift-off velocity might be effective in low-latitude regions. However, the minimum velocity has the same magnitude as that of the ellipsoid model.

3.3 Escape and return velocity

Next, the escape velocity was investigated. A previous study provided the escape velocity in the local normal direction. The escape velocity v_{e} should make the magnitude of the inertial velocity at the surface $\boldsymbol{v}_{\mathrm{I}} = v_{\mathrm{e}}\hat{\boldsymbol{n}} + \boldsymbol{\Omega} \times \boldsymbol{R}$ equal to the critical escape velocity in the two-body problem $v_{\mathrm{c}} = \sqrt{2U_{\max}(\boldsymbol{R})}$, and $U_{\max}(\boldsymbol{R}) = \max(U(\boldsymbol{R}), \mu_{\mathrm{a}}/|\boldsymbol{R}|)$ [41]. Here, $\hat{\boldsymbol{n}}$ is the outer surface normal direction and μ_{a} is the gravity constant of the asteroid. The surface normal velocity is $v_{\mathrm{n}} = \hat{\boldsymbol{n}} \cdot (\boldsymbol{\Omega} \times \boldsymbol{R})$ and the surface tangential velocity is $\boldsymbol{v}_{\mathrm{t}} = \boldsymbol{\Omega} \times \boldsymbol{R} - v_{\mathrm{n}}\hat{\boldsymbol{n}}$. On the leading side, or $v_{\mathrm{n}} > 0$, the surface normal velocity points outwards from the surface, whereas the surface normal velocity points inward from the surface on the tilt side $v_{\mathrm{n}} < 0$. Owing to the fast spin rate of 2016 HO3, the surface velocity itself may be larger than v_{c}. Therefore, three cases can be differentiated:

Case I. If $\|\boldsymbol{v}_{\mathrm{t}}\| > v_{\mathrm{c}}$ or $\|\boldsymbol{v}_{\mathrm{I}}\| > v_{\mathrm{c}}$, $v_{\mathrm{n}} > 0$, changing the velocity along the surface-normal direction cannot reduce the inertial velocity below v_{c}. This means that we cannot determine an escape velocity $v_{\mathrm{e}} \geqslant 0$ on the surface.

Case II. If $\|\boldsymbol{v}_{\mathrm{I}}\| > v_{\mathrm{c}}$, $\|\boldsymbol{v}_{\mathrm{t}}\| < v_{\mathrm{c}}$, and $v_{\mathrm{n}} < 0$, the escape velocity is $v_{\mathrm{e}\max} = |v_{\mathrm{n}}| + \sqrt{2U_{\max}(\boldsymbol{R}) - \|\boldsymbol{v}_{\mathrm{t}}\|^2}$. Meanwhile, a minimum normal velocity is required to avoid escape $v_{\mathrm{e}\min} = |v_{\mathrm{n}}| - \sqrt{2U_{\max}(\boldsymbol{R}) - \|\boldsymbol{v}_{\mathrm{t}}\|^2}$. This implies that an object will escape from the asteroid when $0 < v_{\mathrm{e}} < v_{\mathrm{n}\min}$ or $v_{\mathrm{e}} > v_{\mathrm{n}\max}$.

Case III. If $\|\boldsymbol{v}_{\mathrm{I}}\| < v_{\mathrm{c}}$, the traditional escape velocity is solved as $v_{\mathrm{e}\max} = |v_{\mathrm{n}}| + \sqrt{2U_{\max}(\boldsymbol{R}) - \|\boldsymbol{v}_{\mathrm{t}}\|^2}$. There is no minimum normal velocity or $v_{\mathrm{e}\min} = 0$.

Based on this definition, the escape velocity in 2016 HO3 is shown in Fig. 11. It was found that the escape velocity could only be found near the polar region, and the velocity varied between 0 and 0.027 m/s. Shape model S_2 had a higher velocity than S_1. The minimum normal velocity was found in only one facet of S_2, as shown in Fig. 11. The minimum normal velocity was close to the escape velocity. No such region was found in S_1. The

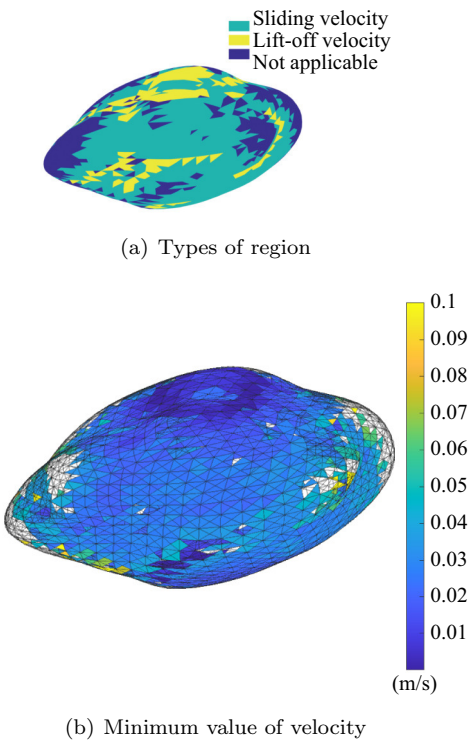

(a) Types of region

(b) Minimum value of velocity

Fig. 10 Lift-off/sliding velocity in the real shape model.

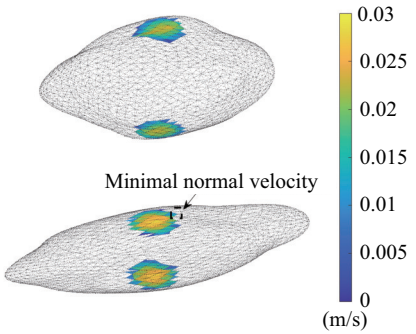

Fig. 11 Escape velocity of the two shape models.

other regions belonged to Case I, and the escape velocity could not be determined. Objects do not require a normal velocity to escape from 2016 HO3.

Furthermore, similar to the lift-off velocity, we revised the escape velocity to determine the range of tangential velocity on the surface to avoid escaping. The inertial velocity at the surface was revised to $\boldsymbol{v}_{\mathrm{I}} = \boldsymbol{v}_{\mathrm{b}} + \boldsymbol{\Omega} \times \boldsymbol{R}$. Here, $\boldsymbol{v}_{\mathrm{b}}$ denotes the velocity in the tangential plane of the local frame. The surfaces can be classified into three types:

Type A: $v_{\mathrm{n}} \geqslant v_{\mathrm{c}}$, and regardless of how we change v_{b}, $\|\boldsymbol{v}_{\mathrm{I}}\|$ is larger than $\sqrt{2U_{\max}(\boldsymbol{R})}$. Similar to Case I, the region belongs to the absolute escape region. Unbound objects will escape from 2016 HO3 at any surface velocity.

Type B: $\|\boldsymbol{v}_{\mathrm{I}}\| > v_{\mathrm{c}}$, but for $v_{\mathrm{n}} < v_{\mathrm{c}}$, we can adjust v_{b} to make the inertial velocity smaller than $\sqrt{2U_{\max}(\boldsymbol{R})}$. The minimum $\boldsymbol{v}_{\mathrm{b\,min}}$ to avoid escaping should be in the opposite direction to $\boldsymbol{v}_{\mathrm{t}}$ and has a magnitude $\|\boldsymbol{v}_{\mathrm{b\,min}}\| = \|\boldsymbol{v}_{\mathrm{t}}\| - \sqrt{2U_{\max}(\boldsymbol{R}) - |v_{\mathrm{n}}|^2}$. In addition, the maximum $\boldsymbol{v}_{\mathrm{b\,max}}$ is also in the opposite direction to $\boldsymbol{v}_{\mathrm{t}}$ and has a magnitude of $\|\boldsymbol{v}_{\mathrm{b\,max}}\| = \|\boldsymbol{v}_{\mathrm{t}}\| + \sqrt{2U_{\max}(\boldsymbol{R}) - |v_{\mathrm{n}}|^2}$. Here, we call $\boldsymbol{v}_{\mathrm{b\,min}}$ and $\boldsymbol{v}_{\mathrm{b\,max}}$ the minimum and maximum return velocities on the surface, respectively. This region is known as the conditional escape region.

Type C: $\|\boldsymbol{v}_{\mathrm{I}}\| < v_{\mathrm{c}}$, the minimum return velocity is $\boldsymbol{v}_{\mathrm{b\,min}} = \boldsymbol{0}$, and the maximum return velocity is the same as that in Type B: $\|\boldsymbol{v}_{\mathrm{b\,max}}\| = \|\boldsymbol{v}_{\mathrm{t}}\| + \sqrt{2U_{\max}(\boldsymbol{R}) - |v_{\mathrm{n}}|^2}$. The region is equal to that of Case III for the escape velocity. We refer to this as the conditional stable region.

The three types of surfaces in the two shape models are shown in Fig. 12. The absolute escape region is shown in dark blue and is close to the major axis. These regions cover both the leading and trailing sides. The cyan region corresponds to the conditional escape region. Objects can avoid escaping if they have a return velocity in a certain direction. The cyan region covers the middle axis and most high-latitude regions, except for the pole. The polar region belongs to the conditional stable region and is presented in yellow. Figure 13 shows the minimum and maximum return velocities for the two shape models.

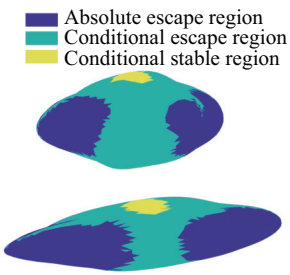

Fig. 12 Escape types of the two models.

Similar to the sliding velocity, the return velocity is constrained in a circular region in a certain direction. Any surface velocity outside the circular region will result in escape. In most regions, the relative Jacobi velocity lies between the minimum and maximum return regions. This means that the particles displaced from the pole may temporally remain in the vicinity if they move to the conditional escape region, but they are likely to escape eventually as the return condition is too strict. It should be noted that the definitions of the escape/returning velocity do not consider the energy change of possible collisions. Collision on a fast-rotating surface may significantly change the inertial velocity, which complicates the escape condition. Because the collision dynamics of an object largely depend on the

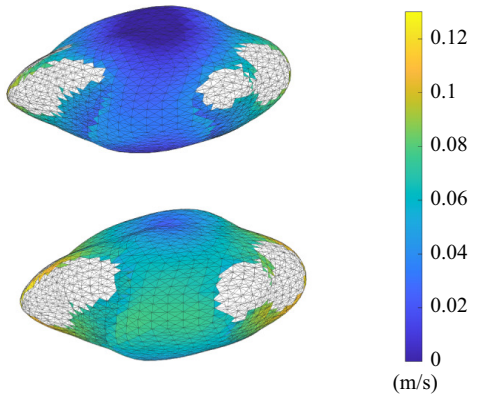

(a) Shape model S_1

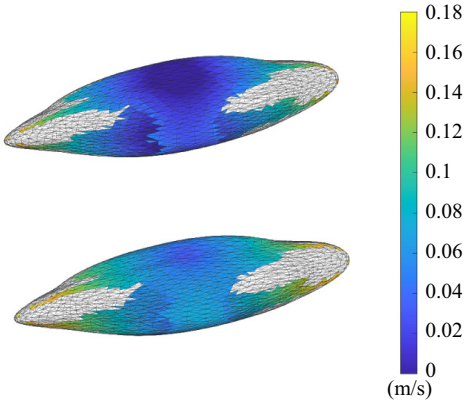

(b) Shape model S_2

Fig. 13 Minimum (top) and maximum (bottom) escape/return velocities of the two shape models.

surface parameters (coefficient of restitution and friction factor), the escape condition under different surface parameters will be further investigated in the future.

By combining the sliding and return velocities, we can obtain indications about how an object moves on the surface of asteroid 2016 HO3. It is interesting to note that the maximum sliding velocity is larger than the maximum return velocity, which means that even sliding on the surface may result in escape. The results show that if we want to operate a lander on the surface of 2016 HO3, the lander needs to control its velocity in time to prevent escape. Meanwhile, any operation should be far from the absolute escape region to avoid unexpected motion.

4 Orbital motion in the asteroid-fixed frame

The above analysis of the geophysical environment of asteroid 2016 HO3 reflects the complicated motions on the surface due to the fast spin rate and elongated shape. These factors also significantly affect the orbital motion in the vicinity of 2016 HO3. Moreover, 2016 HO3 has a small size and weak gravity, and the SRP becomes an unignorable perturbation when examining the orbital motion. The SRP has the same magnitude as gravity when the orbital radius is larger than 100 m. Therefore, we built an equation of motion considering the SRP. SRP acceleration can be expressed as Eq. (2) [22]:

$$\rho_{\mathrm{SRP}} = \frac{c_{\mathrm{r}} P_{\mathrm{SRP}} R_{\mathrm{SRP}}^2}{\sigma R_{\mathrm{s}}^2} \tag{2}$$

Here, $P_{\mathrm{SRP}} = 4.56\ \mu\mathrm{N/m^2}$ denotes the solar pressure at $R_{\mathrm{SRP}} = 1$ AU, c_{r} represents the reflection coefficient, and σ denotes the effective mass-to-area ratio of the spacecraft. R_{s} is the distance from 2016 HO3 to the Sun, which is considered to be a constant.

First, the motion in the asteroid-fixed frame of 2016 HO3 O–XYZ was investigated. Here, the ellipsoid model of 2016 HO3 was used. We adopted the semi-major axis of the ellipsoid model as the length scale, and the reciprocal of the spin rate of 2016 HO3 was taken as a time scale. $\kappa = \rho_{\mathrm{SRP}}/(\omega^2 a R_{\mathrm{s}}^2)$ denotes the normalized SRP. Here a is the semi-major axis of 2016 HO3. For 2016 HO3, κ is in the magnitude of 10^{-4} owing to the high spin rate.

Because the spin period of the asteroid is far smaller than its revolution period, we assume that the Sun is on a circular orbit parallel to the equator plane with a certain latitude λ_{e} and time-varying longitude $\phi_{\mathrm{e}} = -\omega t + \phi_0$ in the asteroid-fixed frame. Here, ϕ_0 is the initial longitude and is set to $\phi_0 = 0$ for simplicity. Then, the direction vector of the Sun becomes

$$\hat{\boldsymbol{R}}_{\mathrm{s}} = \begin{pmatrix} l_x \\ l_y \\ l_z \end{pmatrix} = \begin{pmatrix} \cos\lambda_{\mathrm{e}} \cos\phi_{\mathrm{e}} \\ \cos\lambda_{\mathrm{e}} \sin\phi_{\mathrm{e}} \\ \sin\lambda_{\mathrm{e}} \end{pmatrix} \tag{3}$$

Here, the first order of the SRP acceleration is considered, as it is the major term compared with the gravitational perturbation of the Sun and its second order. Then, the equation in the asteroid-fixed frame becomes [23]:

$$\begin{cases} \ddot{X} - 2\dot{Y} = \dfrac{\partial U}{\partial X} - \nu\kappa \cos\lambda_{\mathrm{e}} \cos\phi_{\mathrm{e}} \\ \ddot{Y} + 2\dot{X} = \dfrac{\partial U}{\partial Y} - \nu\kappa \cos\lambda_{\mathrm{e}} \sin\phi_{\mathrm{e}} \\ \ddot{Z} = \dfrac{\partial U}{\partial Z} - \nu\kappa \sin\lambda_{\mathrm{e}} \end{cases} \tag{4}$$

where ν is the eclipse factor, which can be solved using a cylindrical and conical solar eclipse model [42].

Owing to the fast spin rate, it was found that the equilibrium points in the asteroid-fixed frame were beneath the surface with or without the SRP. Therefore, the natural periodic orbit around the equilibrium does not exist in the vicinity of 2016 HO3, as do the forced periodic orbits when SRP is considered [23]. Retrograde periodic orbits were found around 2016 HO3. Two families of orbits exist at $\lambda_{\mathrm{e}} = 0$. They have similar shapes, but different orbital periods, as shown in Fig. 14. With an increase in the orbital radius, the period of Type 1 family decreases, and the period of Type 2 family increases. However, neither of them equals 2π, which is the period of the Sun in the asteroid-fixed frame. This means that there is a phase difference between the spacecraft and the Sun, which breaks the periodicity. Although the orbit was stable in one period, the SRP perturbation destabilized it after several periods. The orbit gradually diverged and eventually escaped from the system or impacted the surface, driven by the SRP. Figure 15 shows the evolution of a periodic orbit over 60 different periods. The orbit can only remain stable for approximately 30 periods, which is only approximately 0.58 days in real time. If we increase λ_{e}, the periodic orbit is hard to find. One exception is that $\lambda_{\mathrm{e}} = \pi/2$, where stable orbits can be found. It is exactly the terminator orbit in the Sun–asteroid rotating frame. This issue will be discussed later. Given the short rotation period of 2016 HO3, the results show that long-term stable orbits in the asteroid-fixed frame are difficult to find, as both the SRP and acceleration induced by the

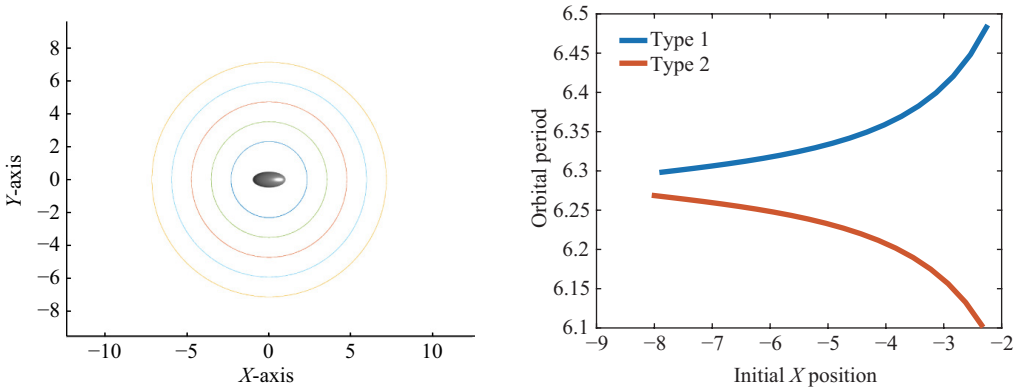

(a) Family of orbits with different radii (b) Orbital period with different radii

Fig. 14 Planar periodic orbits in the asteroid-fixed frame.

fast spin rate seriously affect motions. Frequent orbital maintenance is necessary to offset the influence of the SRP.

5 Orbital motion in the Sun–asteroid rotating frame

Although an stable motion in the asteroid-fixed frame may not exist, we can find stable orbits around 2016 HO3 in the Sun–asteroid rotating frame o-xyz, where the origin of the frame is centered at the asteroid and the x direction points from the Sun to 2016 HO3, the z axis is aligned with the angular velocity of the asteroid, and the y direction completes the right-handed frame. The augmented hill three-body problem (AH3BP) is suitable for describing the motion under the influence of the SRP and solar tides [43]. The equation of motion under the point-mass gravity of the asteroid was first established.

$$\begin{cases} \ddot{x} = 2\omega_{\mathrm{a}}\dot{y} + 3\omega_{\mathrm{a}}^2 x - \dfrac{\mu_{\mathrm{a}} x}{r^3} + \rho_{\mathrm{SRP}} \\ \ddot{y} = -2\omega_{\mathrm{a}}\dot{x} - \dfrac{\mu_{\mathrm{a}} y}{r^3} \\ \ddot{z} = -\omega_{\mathrm{a}}^2 z - \dfrac{\mu_{\mathrm{a}} z}{r^3} \end{cases} \tag{5}$$

where ω_{a} is the orbital angular velocity of 2016 HO3 around the Sun. If we define the normalized length and time unit as $[L] = \left(\frac{\mu_{\mathrm{a}}}{\mu_{\mathrm{s}}}\right)^{\frac{1}{3}} R_{\mathrm{s}}$ and $[T] = \sqrt{\frac{R_{\mathrm{s}}^3}{\mu_{\mathrm{s}}}}$, where μ_{s} is the gravitation parameter of the Sun, a non-dimensional SRP acceleration in the Sun–asteroid rotating frame can be expressed as

$$\beta = \rho_{\mathrm{SRP}} \frac{[T]^2}{[L]} = \frac{c_{\mathrm{r}} P_{\mathrm{SRP}} R_{\mathrm{SRP}}}{\sigma \mu_{\mathrm{s}}^{2/3} \mu_{\mathrm{a}}^{1/3}} \tag{6}$$

A larger SRP parameter β indicates a stronger perturbation caused by the SRP. The mass-to-area ratio

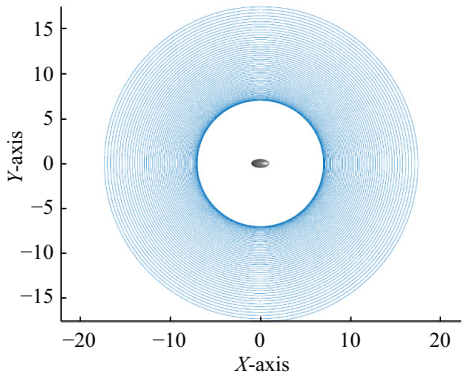

Fig. 15 Evolution of the planar periodic orbit under SRP (60 periods).

of spacecraft σ was selected as 24–80 kg/m^2 with a reflection coefficient $c_{\mathrm{r}} = 1$. For asteroid 2016 HO3 with a mean radius of 18 m and a density of 2.5 g/cm^3, β varies between 300 and 1,000, which is a larger value than that found in previous asteroid missions (β for NEAR at Eros is 0.6, for Hayabusa at Itokawa is 97, for OSIRIS-Rex at Bennu is 33, and for Hayabusa 2 at Ryugu is 35) [43]. This means that the SRP has a greater influence on the motion near 2016 HO3 than that for other asteroids.

5.1 Periodic orbits in the AH3BP

Previous research has found that a stable terminator orbit exists in the Sun–asteroid rotating frame. Its orbital plane is always perpendicular to the Sun–asteroid line, and the orbit center is slightly offset from the asteroid center along the Sun–asteroid direction. The initial guess of terminator orbits can be determined by a grid search. Because of the symmetry of the dynamics, the terminator orbit should be symmetric with the xz plane. This provides

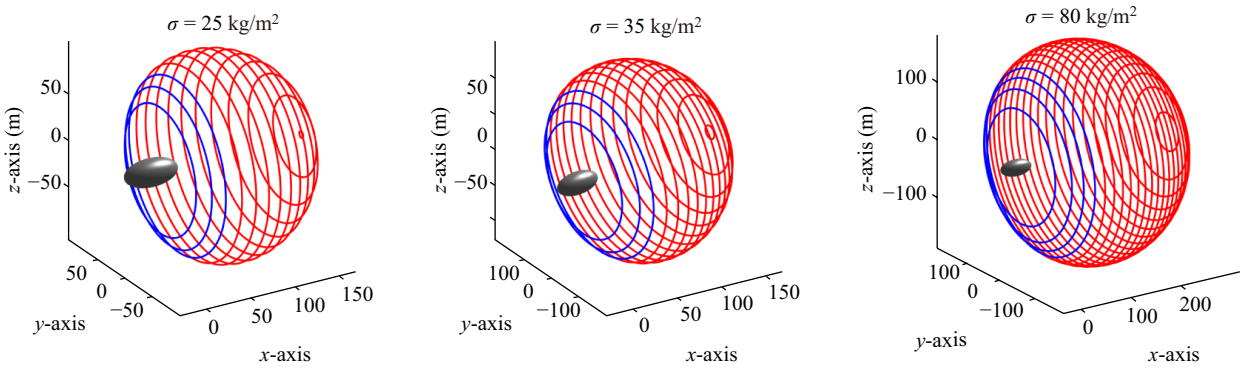

Fig. 16 Terminator orbits around 2016 HO3 with different σ.

the constraints for the differential corrector. Once one terminator orbit is found, the family of terminator orbits can be obtained using the continuation method. The continuation method was also used to gradually change the SRP parameter. Moreover, the stability of terminator orbits was solved by the eigenvalue of the monodromy matrix [44] in the form of $[\lambda_1, 1/\lambda_1, \lambda_2, 1/\lambda_2, 1, 1]$. Here, the stability index ν_s was used [45]:

$$\nu_s = \frac{1}{2}\left|\lambda_{\max} + \frac{1}{\lambda_{\max}}\right| \tag{7}$$

$\lambda_{\max}$ denotes the maximum eigenvalue. If $\nu_s \leqslant 1$, the orbit is considered stable. The larger the stability index, the more susceptible the orbit is to disturbances.

The terminal orbit near asteroid 2016 HO3 was investigated at different σ values. Figure 16 shows the results for different offsets along the x-axis. The point-mass gravity of 2016 HO3 is used. However, a shape model is presented to compare the size. The stable orbit is shown in blue and the unstable orbit is shown in red. The stable orbits are close to those of 2016 HO3. The radius of the terminator orbit first increases and then decreases as the center of orbit moves away from asteroid 2016 HO3. The radius of the stable orbit is between 25 and 50 m for $\sigma = 25$ kg/m^2 and increases to 100 m for $\sigma = 80$ kg/m^2. Finally, the orbit is convergent to equilibrium in the Sun–asteroid rotating frame.

Figure 17 shows the stability index of terminator orbits with different offsets and mass-to-area ratios. A smaller σ means a larger SRP acceleration. As can be observed, the offset of stable orbits is less than 50 m. In the meantime, at the same offset, an increase in σ leads to a smaller stability index. Figure 18 shows the orbital period of different terminal orbits. The period ranges from 0.6 to 5 days. A larger σ and larger offset tend to a longer period.

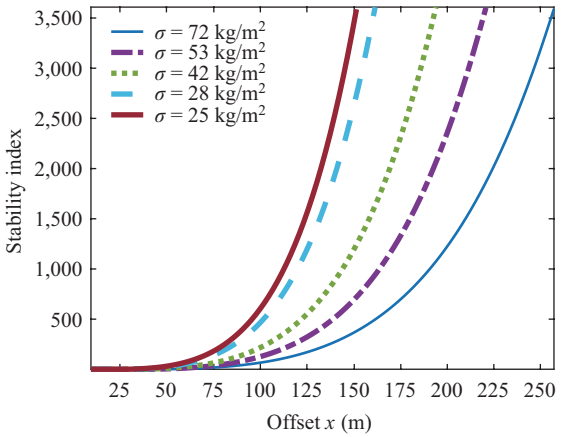

Fig. 17 Stability index of terminator orbit.

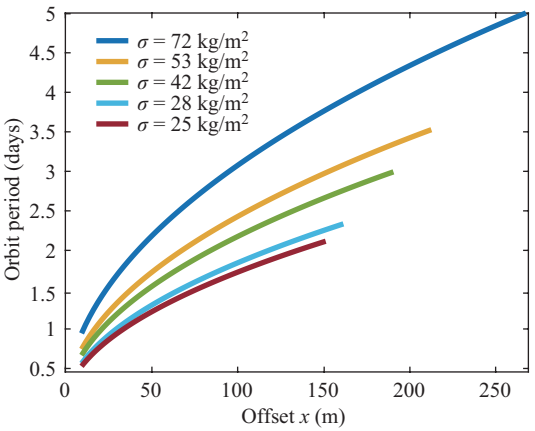

Fig. 18 Stability index of terminator orbit.

For the stable orbits, the orbit period varies between 0.6 and 2.3 days. Figure 19 compares the terminal orbits with different σ and with the same offset. The SRP parameter β is inversely proportional to σ. Therefore, orbits with larger β are closer to the asteroid.

In addition to the single-period terminator orbit, quasi-terminator orbits can also be found near asteroid 2016

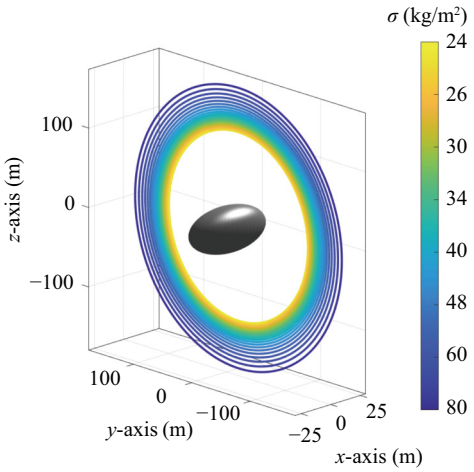

Fig. 19 Terminator orbits at different σ (offset: 5 m).

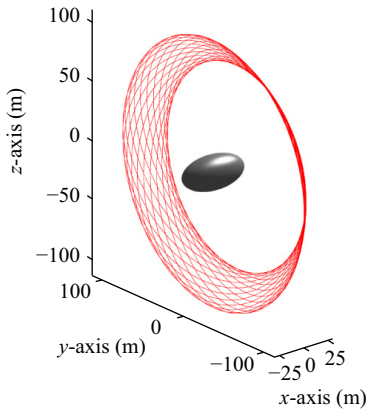

(a) Quasi-terminator orbit near asteroid 2016 HO3

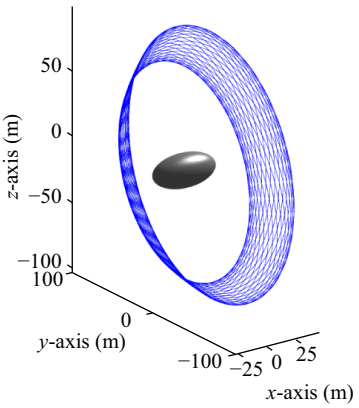

(b) Dark-side orbit

Fig. 20 Quasi-terminator orbits near asteroid 2016 HO3.

HO3 [43]. They can be built using the two-dimensional (2D) invariant torus of terminal orbits. Figure 20 shows two examples. There are two types of terminator orbits based on different stable eigenvalues. The Sun-side quasi-terminator orbits will curve in the direction of the Sun, and the dark-side quasi-terminator orbits will extend away along the x direction. Compared with terminal orbits, quasi-terminator orbits cover more regions with the same stability. These are also options for mission orbits.

Meanwhile, based on grid searching, more periodic orbits can be found in the frame of AH3BP, including periodic orbits near equilibrium, as shown in Fig. 21. The orbits look like arcs and extend mostly in the y direction. They do not move around the equilibrium but are located on the asteroid side. The stability indices of these orbits are larger than 3,000, indicating poor stability. Most of the periodic orbits in AH3BP are unstable and unsuitable for mission orbits. Because periodic orbits are sensitive to parameters, a thorough search might be interesting once the physical parameters of the asteroid and spacecraft are determined.

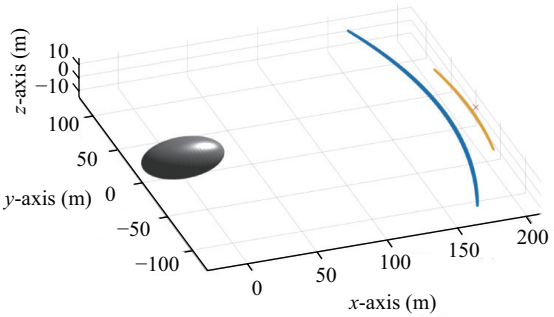

Fig. 21 Periodic orbit near equilibrium in AH3BP.

5.2 Influence of irregular shape perturbation

In AH3BP, the irregular-shape of an asteroid has not been considered. Because of the weak gravity of 2016 HO3, the terminator orbits are very close to the surface, which makes the non-spherical perturbation non-negligible, especially for an extremely elongated shape. Therefore, the influence of the non-spherical shape on the terminator orbits was examined. The orientation of the spin axis can be determined using two angles, α and γ. Here, γ is the angle between the spin axis and xy plane. α is the angle between the projection of the spin axis in the xy-plane and the x-axis. As 2016 HO3 revolves around the Sun, the spin axis rotates clockwise along the z-axis over a period of one year. The direction vector of the spin axis is $\hat{\boldsymbol{l}} = [\cos\alpha(t)\cos\gamma, \sin\alpha(t)\cos\gamma, \sin\gamma]$. $\alpha(t) = \alpha_0 - \omega_a t$. Another angle θ was defined to describe the rotation angle with respect to the spin rate. The transfer matrix

$\boldsymbol{R}_{\rm M}$ from the Sun–asteroid frame to the asteroid-fixed frame is as Eq. (8):

$$\boldsymbol{R}_{\rm M} = \boldsymbol{R}_z(\theta)\boldsymbol{R}_y\left(\frac{\pi}{2}-\gamma\right)\boldsymbol{R}_z(\alpha) \tag{8}$$

Here, $\boldsymbol{R}_y$ and $\boldsymbol{R}_z$ are rotation matrices along the y and z axes, respectively. The rotation angle was $\theta = \theta_0 + \omega t$.

The numerical simulation shows that if a non-spherical perturbation is considered, the stable terminator orbit is seriously perturbed and the unstable terminator orbit may escape from nearby within one period. Figure 22 gives two examples. Here the ellipsoid gravity model is used and the size ratio S_2 is selected. The orientation of the spin axis is chosen as $\alpha_0 = 0, \gamma = \pi/2$, and $\theta_0 = 0$. The mass-to-area ratio is $\sigma = 50$ kg/m^2.

The terminator orbit is no longer periodic when the shape perturbation of the asteroid is considered. In fact, a strict periodic orbit may not be able to be found, as the orbit period will be different from the spin period of the asteroid in general. However, the stable terminator orbit can still be bound to a narrow region using certain techniques. Here, we define a virtual periodic terminator orbit (different from the quasi-terminator orbit) under the following assumptions.

First, the period of the virtual periodic terminator orbits is far smaller than the orbital period of 2016 HO3 around the Sun. Therefore, we assume that the spin axis does not change direction in a rotating frame in a short time. Second, the spin period of 2016 HO3 is far smaller than that of the non-perturbed terminator orbits. Hence, we consider that an orbit is virtual periodic if it starts and ends at the same points with the same velocity in the Sun–asteroid frame and the difference in the rotation angle θ at the initial and terminal moments is ignored.

The asymmetric correction algorithm, which has been used to find periodic orbits at the $L4/L5$ points in the circular-restricted three-body problem (CRTBP), is applied here [46]. We assume that an orbit starts on the yz plane and $y = 0$ is used as the index variable to design the orbits. The initial states of the orbit are $\boldsymbol{X}_0 = [x_0, 0, z_0, \dot{x}_0, \dot{y}_0, \dot{z}_0]$. Based on this assumption, the orientation of the asteroid is fixed at α_0 and γ. The initial rotation angle is arbitrarily chosen as θ_0. The orbit ends at $\boldsymbol{X}_{\rm f} = [x_{\rm f}, 0, z_{\rm f}, \dot{x}_{\rm f}, \dot{y}_{\rm f}, \dot{z}_{\rm f}]$, when $\dot{y}_0 \cdot \dot{y}_{\rm f} > 0$. The virtual periodic conditions are $x_0 = x_{\rm f}, z_0 = z_{\rm f}, \dot{x}_0 = \dot{x}_{\rm f}, \dot{y}_0 = \dot{y}_{\rm f}$, and $\dot{z}_0 = \dot{z}_{\rm f}$. We only need to build the equation for four variables, and the last one is constrained automatically by the integral of the orbital energy. Here, variables $x, z, \dot{x}$, and $\dot{z}$ are chosen. The goal is to eliminate the variations $\delta x, \delta\dot{x}, \delta z, \delta\dot{z}$ and find a virtual-periodic orbit.

$$\begin{cases} F(x_0+\delta x_0, z_0+\delta z_0, \dot{x}_0+\delta\dot{x}_0, \dot{z}_0+\delta\dot{z}_0, \dot{y}_0+\dot{y}_0) \\ \quad = x_0 + \delta x_0 \\ G(x_0+\delta x_0, z_0+\delta z_0, \dot{x}_0+\delta\dot{x}_0, \dot{z}_0+\delta\dot{z}_0, \dot{y}_0+\dot{y}_0) \\ \quad = z_0 + \delta z_0 \\ H(x_0+\delta x_0, z_0+\delta z_0, \dot{x}_0+\delta\dot{x}_0, \dot{z}_0+\delta\dot{z}_0, \dot{y}_0+\dot{y}_0) \\ \quad = \dot{x}_0 + \delta\dot{x}_0 \\ I(x_0+\delta x_0, z_0+\delta z_0, \dot{x}_0+\delta\dot{x}_0, \dot{z}_0+\delta\dot{z}_0, \dot{y}_0+\dot{y}_0) \\ \quad = \dot{z}_0 + \delta\dot{z}_0 \end{cases} \tag{9}$$

By Taylor expansion to the first order, it has

$$\begin{Bmatrix} \delta x \\ \delta z \\ \delta\dot{x} \\ \delta\dot{z} \end{Bmatrix} = (\boldsymbol{Q}-\boldsymbol{P}) \begin{Bmatrix} \delta x_0 \\ \delta z_0 \\ \delta\dot{x}_0 \\ \delta\dot{y}_0 \\ \delta\dot{z}_0 \end{Bmatrix} \tag{10}$$

where

$$\boldsymbol{Q} = \begin{bmatrix} \frac{\partial F}{\partial x_0} & \frac{\partial F}{\partial z_0} & \frac{\partial F}{\partial \dot{x}_0} & \frac{\partial F}{\partial \dot{y}_0} & \frac{\partial F}{\partial \dot{z}_0} \\ \frac{\partial G}{\partial x_0} & \frac{\partial G}{\partial z_0} & \frac{\partial G}{\partial \dot{x}_0} & \frac{\partial G}{\partial \dot{y}_0} & \frac{\partial G}{\partial \dot{z}_0} \\ \frac{\partial H}{\partial x_0} & \frac{\partial H}{\partial z_0} & \frac{\partial H}{\partial \dot{x}_0} & \frac{\partial H}{\partial \dot{y}_0} & \frac{\partial H}{\partial \dot{z}_0} \\ \frac{\partial I}{\partial x_0} & \frac{\partial I}{\partial z_0} & \frac{\partial I}{\partial \dot{x}_0} & \frac{\partial I}{\partial \dot{y}_0} & \frac{\partial I}{\partial \dot{z}_0} \end{bmatrix}$$

$$\boldsymbol{P} = \begin{bmatrix} 1 & 0 & 0 & 0 & 0 \\ 0 & 1 & 0 & 0 & 0 \\ 0 & 0 & 1 & 0 & 0 \\ 0 & 0 & 0 & 0 & 1 \end{bmatrix}$$

Then, based on the first-order approximation for the variation δX,

$$\delta X = \Phi\delta X_0 + \dot{X}\delta t \tag{11}$$

$\boldsymbol{Q}$ is rewritten as

$$\boldsymbol{Q} = \begin{bmatrix} \frac{\partial x}{\partial x_0} & \frac{\partial x}{\partial z_0} & \frac{\partial x}{\partial \dot{x}_0} & \frac{\partial x}{\partial \dot{y}_0} & \frac{\partial x}{\partial \dot{z}_0} \\ \frac{\partial y}{\partial x_0} & \frac{\partial y}{\partial z_0} & \frac{\partial y}{\partial \dot{x}_0} & \frac{\partial y}{\partial \dot{y}_0} & \frac{\partial y}{\partial \dot{z}_0} \\ \frac{\partial \dot{x}}{\partial x_0} & \frac{\partial \dot{x}}{\partial z_0} & \frac{\partial \dot{x}}{\partial \dot{x}_0} & \frac{\partial \dot{x}}{\partial \dot{y}_0} & \frac{\partial \dot{x}}{\partial \dot{z}_0} \\ \frac{\partial \dot{z}}{\partial x_0} & \frac{\partial \dot{z}}{\partial z_0} & \frac{\partial \dot{z}}{\partial \dot{x}_0} & \frac{\partial \dot{z}}{\partial \dot{y}_0} & \frac{\partial \dot{z}}{\partial \dot{z}_0} \end{bmatrix} - \frac{1}{\dot{y}} \begin{Bmatrix} \dot{x} \\ \dot{z} \\ \ddot{x} \\ \ddot{z} \end{Bmatrix} \begin{bmatrix} \frac{\partial y}{\partial x_0} & \frac{\partial y}{\partial z_0} & \frac{\partial y}{\partial \dot{x}_0} & \frac{\partial y}{\partial \dot{y}_0} & \frac{\partial y}{\partial \dot{z}_0} \end{bmatrix} \tag{12}$$

The initial state vector of a terminal orbit in AH3BP is used as the initial guess and updated via $\delta x_0, \delta z_0, \delta\dot{x}_0, \delta\dot{y}_0, \delta\dot{z}_0$ in an iterative process until $\delta x_0, \delta z_0, \delta\dot{x}_0, \delta\dot{z}_0 < \varepsilon$ to find a virtual-periodic terminator orbit in the real shape model.

By correction, the orbit was closed only during the first period. As the rotation angle θ changed in each turn, small deviations existed in the following orbital periods.

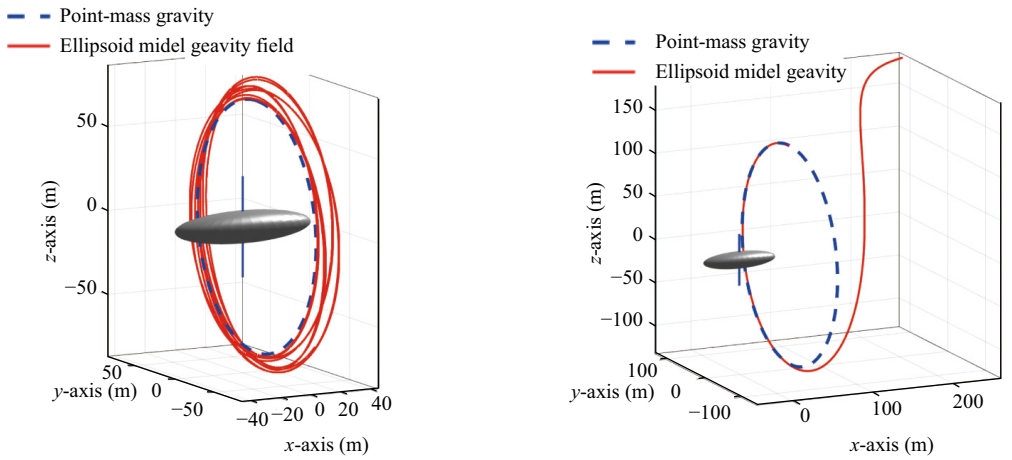

(a) Stable orbit (b) Unstable orbit

Fig. 22 Terminator orbits under non-spherical perturbation ($\alpha_0 = 0, \gamma = \pi/2, \theta_0 = 0, \sigma = 50$ kg/m^2).

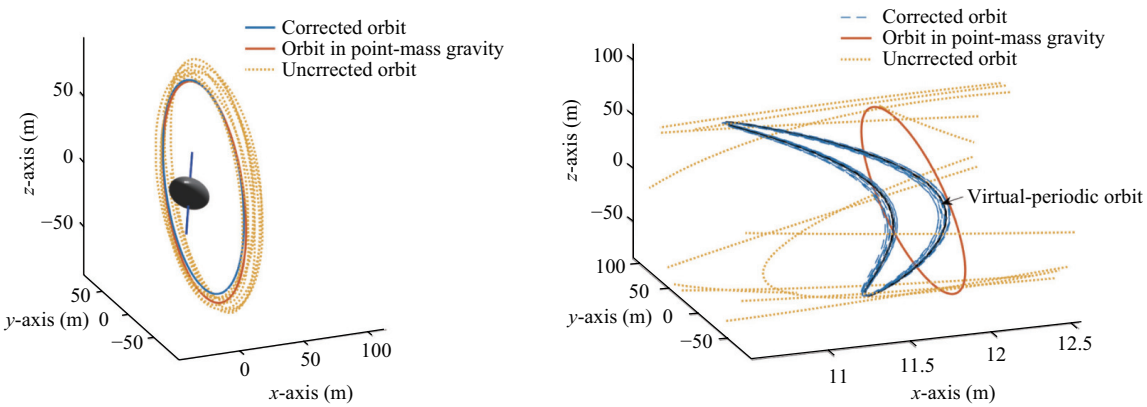

(a) Global view (b) Local view

Fig. 23 Virtual-periodic terminator orbits under non-spherical perturbation ($\alpha_0 = \pi/3, \gamma = \pi/3, \theta_0 = 0, \sigma = 50$ kg/m^2).

However, the stability analysis shows that the virtual periodic orbit is still a stable orbit. The small error did not diverge over multiple periods. The numerical calculations are shown in Fig. 23. Here, the orbit is integrated for ten periods with initial states $\alpha_0 = \pi/3, \gamma = \pi/3, \theta_0 = 0, \sigma = 50$ kg/m^2. The corrected orbit was bound and moved close to the virtual periodic orbit. Compared with the uncorrected orbit, the corrected orbit remained nearly in the same plane as the terminator orbit in AH3BP. A close-up image shows that the bounded orbit becomes a spatial curve. It bends and twists owing to perturbations.

The evolutions of the virtual periodic orbits at different initial rotation angles $\theta_0 = 0, \pi/6, \pi/3, \pi/2, 2\pi/3$, and $5\pi/6$ are shown in Fig. 24. The virtual periodic orbit was solved at $\theta_0 = 0$. The virtual periodic orbit was found to be insensitive to the initial rotation angle θ_0. Because of the fast spin rate of 2016 HO3, the spacecraft moves in a short arc on orbit in one spin period. Therefore, the average perturbation force in one spin period for the same orbital segment was similar for all situations. The maximum position error was less than 0.5 m, which can be neglected compared with the orbital radius of approximately 80 m.

Compared to the rotation angle, the orientation of the spin axis had a greater impact on the terminator orbit. The influence of rotation angle θ was limited. The initial rotation angle was set to $\theta_0 = 0$. Here, we adopted different pole orientations of the triaxial ellipsoid model in the Sun–asteroid rotating frame. By correction, the virtual periodic terminator orbits were compared with the terminator orbits in the AH3BP, as shown in Fig. 25. The virtual periodic terminator orbit is shown as a solid

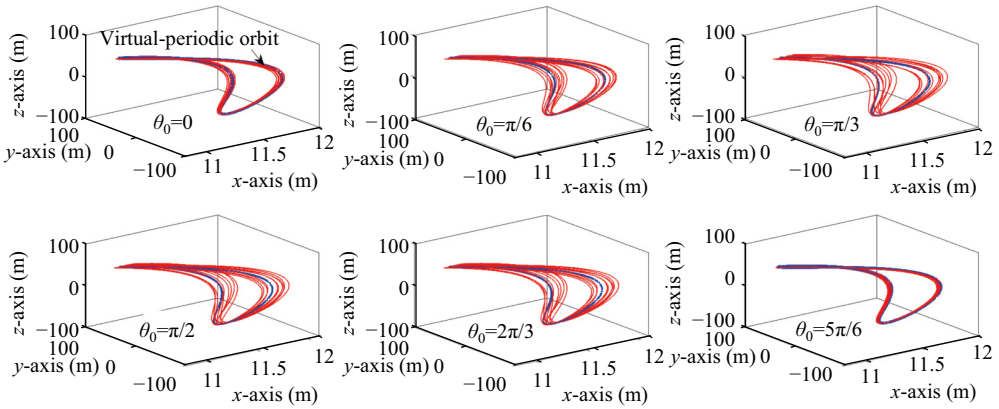

Fig. 24 Evolutions of virtual-periodic orbits at different initial rotation angles.

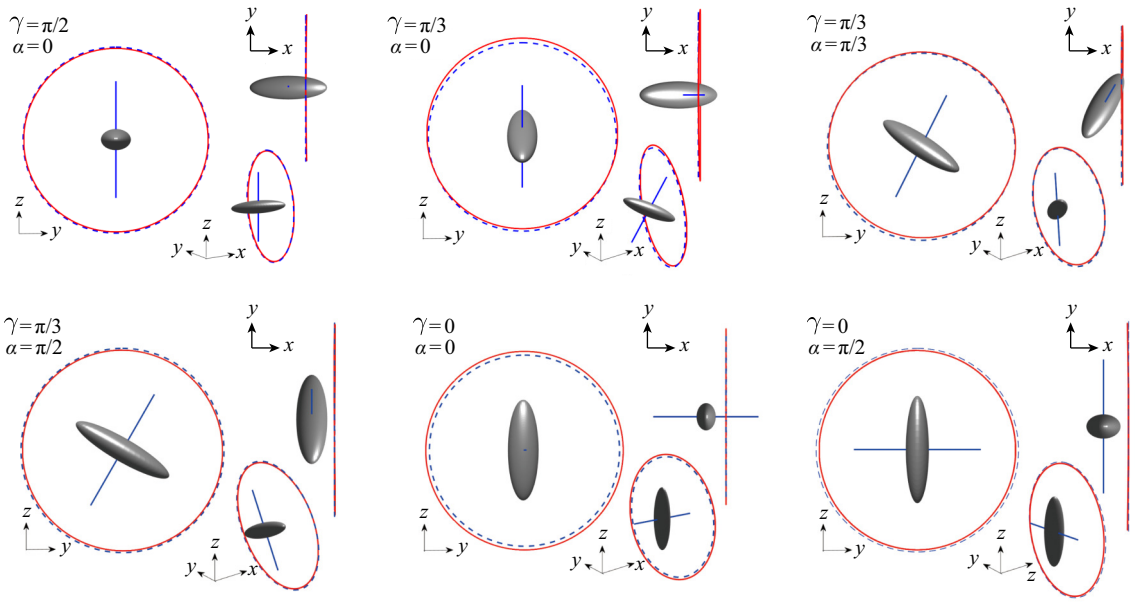

Fig. 25 Influence of pole orientation on terminator orbits (solid line: virtual-periodic terminator orbits in the shape model; dash line: terminator orbit in the point mass model).

line, and the terminator orbit in the point-mass model is shown as a dashed line. The spin axes are shown in each plot. As can be observed, the differences are reflected in two aspects: the change in size and offset of the orbit center.

Two types of average perturbation accelerations are defined. The spin-average perturbation is the average perturbation acceleration at point P in one spin period of the asteroid:

$$\Delta \boldsymbol{a}_{\mathrm{s}}(\boldsymbol{r}) = \frac{1}{2\pi}\int_0^{2\pi}\left(\frac{\partial U(\theta)}{\partial \boldsymbol{r}} - \frac{\mu_{\mathrm{a}}}{\|\boldsymbol{r}\|^3}\boldsymbol{r}\right)\mathrm{d}\theta \tag{13}$$

Here, $U(\theta)$ is the gravitational potential function at the rotation angle θ.

Integrating the spin-average perturbation along orbit Γ in one orbital period T, we obtained the orbital-average perturbation:

$$\Delta \boldsymbol{a}_{\mathrm{o}} = \frac{1}{T}\int_0^{\mathrm{T}} \Delta \boldsymbol{a}_{\mathrm{s}}(\boldsymbol{r}(t))\mathrm{d}t,\ \ \boldsymbol{r}(t)\in\Gamma \tag{14}$$

The change in size was noticeable at $\gamma = 0$, $\alpha = 0$, and $\gamma = 0, \alpha = \pi/2$. The spin axis was parallel to the x and y axes. The spin-average perturbation $\Delta \boldsymbol{a}_{\mathrm{s}}$ was symmetric along the xz and xy planes. Therefore, $\Delta \boldsymbol{a}_{\mathrm{o}}$ should be close to zero, and the center of the orbit should not change in the yz plane. However, the elongated shape changed the average gravitational acceleration along the three axes. For pole orientations $\gamma = 0$ and $\alpha = 0$, it

has $\Delta a_{ox} > 0$. In addition, $\Delta a_{oy} y < 0$ and $\Delta a_{oz} z < 0$. Therefore, the current system is equivalent to a system in which the asteroid has a larger mass but the SRP decreases, which results in a smaller β. Therefore, as shown in Fig. 19, the orbit radius will increase if the offset of the orbit center along the x-axis does not change. For the pole orientation of $\gamma = 0, \alpha = \pi/2$, opposite results were obtained, which corresponded to a system with a larger SRP parameter. The radius of the terminator orbit was reduced. A similar situation occurred at $\gamma = \pi/2, \alpha = 0$. In other situations, $\Delta \boldsymbol{a}_{\mathrm{s}}$ was not symmetric along the xz or xy plane. Therefore, a peculiar disturbance acceleration Δa_{oy} or Δa_{oz} existed, which offset the orbit center in the yz plane. The offset direction is related to the pole direction and may be incorporated into the size change. Nevertheless, the virtual periodic terminator orbit was still close to the nominal orbit in all situations. The maximum deviation was less than 5 m, which is a tolerable value compared to the orbital radius.

The above correction process can be used to find the virtual periodic orbit when a real-shape model of the asteroid is applied. However, calculations based on a shape model, such as the polyhedron method, are time-consuming and the convergence is difficult. Therefore, based on the above analysis, we developed a new method for designing a virtual-periodic orbit around a non-spherical small body using the average perturbation acceleration $\Delta \boldsymbol{a}_{\mathrm{s}}$.

The terminator orbit in the point-mass model $\Gamma_0(\boldsymbol{r}(t), \boldsymbol{v}(t))$ was selected as the initial estimate. Using Eq. (13), the spin-average perturbation acceleration along the orbit Γ was calculated as $\Delta \boldsymbol{a}_{\mathrm{s}}(\boldsymbol{r}(t) \in \Gamma_0)$ and added to Eq. (5):

$$\begin{cases} \ddot{x} = 2\omega_{\mathrm{a}}\dot{y} + 3\omega_{\mathrm{a}}^2 x - \dfrac{\mu_{\mathrm{a}} x}{r^3} + \rho_{\mathrm{SRP}} + \Delta a_{\mathrm{s}x} \\ \ddot{y} = -2\omega_{\mathrm{a}}\dot{x} - \dfrac{\mu_{\mathrm{a}} y}{r^3} + \Delta a_{\mathrm{s}y} \\ \ddot{z} = -\omega_{\mathrm{a}}^2 z - \dfrac{\mu_{\mathrm{a}} z}{r^3} + \Delta a_{\mathrm{s}z} \end{cases} \tag{15}$$

An asymmetric differential corrector was applied based on Eq. (15) to find a virtual-periodic orbit Γ_1. Γ_1 and Γ_0 may have errors in the position and period, which results in an inaccurate $\Delta \boldsymbol{a}_{\mathrm{s}}$ in Eq. (15). Γ_1 was integrated for one period in the real gravitational field, and the difference between the initial and terminal states was denoted as ΔX_1. If ΔX was larger than the critical threshold ε_{p}, Γ_1 was considered a new initial estimate for calculating the spin-average perturbation acceleration and starting the correction process until $\Delta X_i < \varepsilon_{\mathrm{p}}$ ($i = 1, 2, 3, \cdots, m$). Through iterations, orbit Γ_m was obtained as the virtual periodic orbit in the real gravitational field. As the gravity field of the shape model was replaced by a time-variant function $\Delta \boldsymbol{a}_{\mathrm{s}}$ in the correction process, the efficiency was significantly improved. In general, if we set $\varepsilon_{\mathrm{p}} = 0.1$, the virtual periodic terminator orbit can be found in less than eight iterations. Figure 26 shows an example with the parameters $\sigma = 50$ kg/m^2, $\gamma = \pi/3$, $\alpha = \pi/6$, $\theta_0 = 0$. The corrected orbit was solved using Eq. (15), while the uncorrected orbit was the original terminate orbit in the point-mass model. The revised orbit was well-bounded in multiple periods, even in a complicated gravitational field.

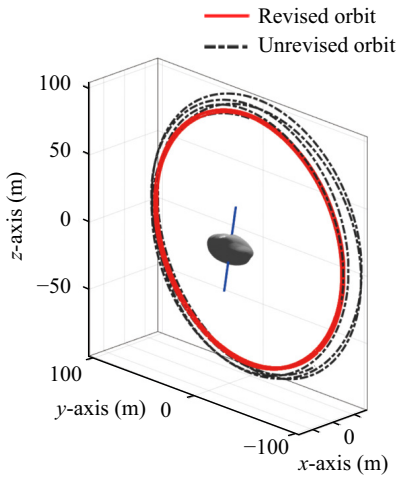

Fig. 26 Virtual-periodic terminator orbits in the real shape model.

5.3 Terminator orbits in the high-fidelity model

Finally, we transferred the solution in the Sun–asteroid rotating frame to the inertial frame to investigate the stability of terminator orbits in the ephemeris model of 2016 HO3 [13]. The initial time was selected as January 1, 2026. The axis orientation was chosen as $\gamma = \pi/3, \alpha = \pi/3$ in the initial rotating frame. The radius of the terminator orbit was approximately 93.7 m. The orbit was revised in a real-shape gravity field, as mentioned above. Figure 27 shows the evolution of a terminator orbit over one year. The orbits in both inertial and rotating frames are presented. As can be observed, the revised terminator orbit shows good stability in the ephemeris model. The orbit will neither escape from 2016

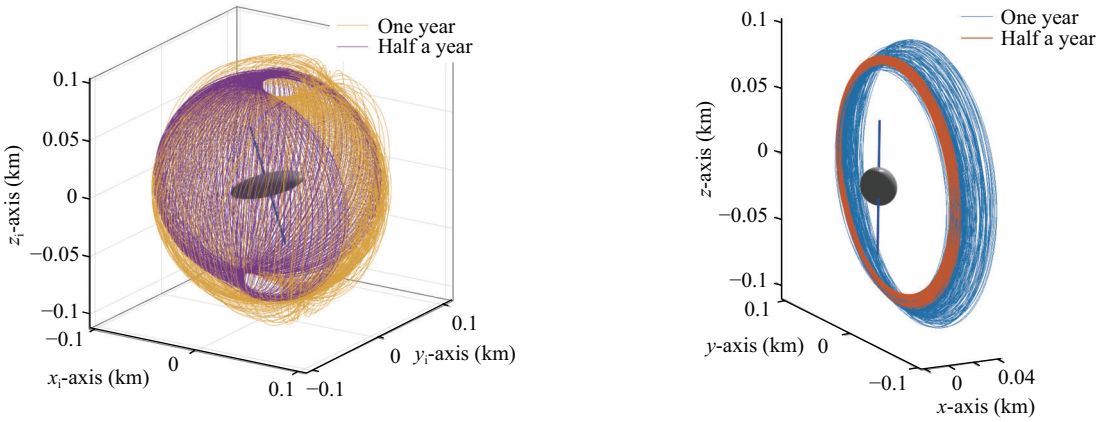

(a) Inertial frame

(b) The Sun–asteroid rotating frame

Fig. 27 Evolution of a terminator orbit in the ephemeris model of 2016 HO3.

HO3 nor impact the surface in one year. In particular, the orbit is well bounded for at least 250 days. As the orbit of 2016 HO3 is not a perfect circle ($e = 0.1$), the effect of SRP will increase when the asteroid is near the periapsis and decrease when it moves to the apoapsis. Therefore, when 2016 HO3 is close to its periapsis (perihelion moment October 6, 2026), a strong SRP pushes the terminator orbit away from the asteroid, as shown in Fig. 27(b). However, the orbit can remain stable as long as the offset of the orbit center is within the stable region (see Fig. 17). In contrast, the uncorrected terminal orbit based on the point-mass model is more sensitive to the change in SRP, as the orbit fluctuates in a large space owing to irregular-shape gravity perturbation. The orbit escapes from 2016 HO3 in less than half a year. The results indicate that the precise orbit design in Section 5.2 is necessary, as it improves the orbital stability against perturbations and reduces the frequency of orbital maintenance.

6 Conclusions

In this study, the geophysical and orbital environments of asteroid 2016 HO3 were investigated. Asteroid 2016 HO3 is a potential target for future exploration. However, its fast spin rate, weak gravity, and elongated shape make the dynamic environment of 2016 HO3 significantly different from those of planets and other explored small bodies. First, the geometric and geopotential topographies of 2016 HO3 were examined based on shape and ellipsoid models with different size ratios. Owing to the fast spin rate, the geometric and geopotential topographies differ over the entire surface. The surface slope is less than 90° only near the polar regions. The elongated shape aggravates the disparity in the geopotential over the surface. Subsequently, the lift-off and escape velocities on the surface were investigated. The polar region was determined as the primary region for landing or sampling. Objects in other regions require tangential velocity along a certain direction to avoid lifting off or escape. The surface was classified, and the ranges of the sliding and returning velocities were solved. Then, the orbital motion around 2016 HO3, considering the SRP, was investigated. No stable orbit was observed in the fixed asteroid frame. However, stable terminator orbits exist in the Sun–asteroid rotating frame. The stability and range of terminator orbits with different parameters were investigated. The influence of the nonspherical perturbation on the terminator orbits was analyzed. In particular, a numerical method was proposed to determine the precise terminator orbits in real shape models. Finally, simulations in the high-fidelity model of 2016 HO3 showed that terminator orbits are stable over perturbations, which is an ideal option for target orbits in exploration missions. The analysis and orbit design in this study can serve as references for future landing or rendezvous exploration of asteroid 2016 HO3 or small bodies with similar characteristics.

Acknowledgements

The authors acknowledge support from the National Natural Science Foundation of China (Grant Nos. 12002028 and 51827806), Beijing Institute of Technology

Research Fund Program for Young Scholars, China Postdoctoral Science Foundation funded project (Grant No. 2019QT0038), and Ann and H. J. Smead Aerospace Engineering Science Department, University of Colorado Boulder.

Declaration of competing interest

The authors have no competing interests to declare that are relevant to the content of this article.

References

[1] Veverka, J., Farquhar, B., Robinson, M., Thomas, P., Murchie, S., Harch, A., Antreasian, P. G., Chesley, S. R., Miller, J. K., Owen, W. M., *et al.* The landing of the NEAR-shoemaker spacecraft on asteroid 433 Eros. *Nature*, **2001**, 413(6854): 390–393.

[2] Yano, H., Kubota, T., Miyamoto, H., Okada, T., Scheeres, D., Takagi, Y., Yoshida, K., Abe, M., Abe, S., Barnouin-Jha, O., *et al.* Touchdown of the Hayabusa spacecraft at the Muses Sea on Itokawa. *Science*, **2006**, 312(5778): 1350–1353.

[3] Russell, C. T., Raymond, C. A., Coradini, A., McSween, H. Y., Zuber, M. T., Nathues, A., de Sanctis, M. C., Jaumann, R., Konopliv, A. S., Preusker, F., *et al.* Dawn at Vesta: Testing the protoplanetary paradigm. *Science*, **2012**, 336(6082): 684–686.

[4] Walsh, K. J., Jawin, E. R., Ballouz, R. L., Barnouin, O. S., Bierhaus, E. B., Connolly, H. C., Molaro, J. L., McCoy, T. J., Delbo', M., Hartzell, C. M., *et al.* Craters, boulders and regolith of (101955) Bennu indicative of an old and dynamic surface. *Nature Geoscience*, **2019**, 12(4): 242–246.

[5] Watanabe, S., Hirabayashi, M., Hirata, N., Hirata, N., Noguchi, R., Shimaki, Y., Ikeda, H., Tatsumi, E., Yoshikawa, M., Kikuchi, S., *et al.* Hayabusa2 arrives at the carbonaceous asteroid 162173 Ryugu—A spinning top-shaped rubble pile. *Science*, **2019**, 364(6437): 268–272.

[6] Takao, Y., Mimasu, Y., Tsuda, Y. Simultaneous estimation of spacecraft position and asteroid diameter during final approach of Hayabusa2 to Ryugu. *Astrodynamics*, **2020**, 4(2): 163–175.

[7] Tsuda, Y., Takeuchi, H., Ogawa, N., Ono, G., Kikuchi, S., Oki, Y., Ishiguro, M., Kuroda, D., Urakawa, S., Okumura, S. I., *et al.* Rendezvous to asteroid with highly uncertain ephemeris: Hayabusa2's Ryugu-approach operation result. *Astrodynamics*, **2020**, 4(2): 137–147.

[8] Hart, W., Brown, G. M., Collins, S. M., de Soria-Santacruz Pich, M., Fieseler, P., Goebel, D., Marsh, D., Oh, D. Y., Snyder, S., Warner, N., *et al.* Overview of the spacecraft design for the Psyche mission concept. In: Proceedings of the 2018 IEEE Aerospace Conference, Big Sky, MT, USA, **2018**.

[9] Levison, H. F., Olkin, C., Noll, K. S., Marchi, S., Team, L. Lucy: Surveying the diversity of the Trojan Asteroids: The fossils of planet formation. In: Proceedings of the 48th Lunar and Planetary Science Conference, the Woodlands, Texas, USA, **2017**: 2025.

[10] Michel, P., Cheng, A., Küppers, M., Pravec, P., Blum, J., Delbo, M., Green, S. F., Rosenblatt, P., Tsiganis, K., Vincent, J. B., *et al.* Science case for the asteroid impact mission (AIM): A component of the asteroid impact & deflection assessment (AIDA) mission. *Advances in Space Research*, **2016**, 57(12): 2529–2547.

[11] Hergenrother, C. W., Whiteley, R. J. A survey of small fast rotating asteroids among the near-Earth asteroid population. *Icarus*, **2011**, 214(1): 194–209.

[12] Harris, A. W. The rotation rates of very small asteroids: Evidence for "Rubble Pile" structure. In: Proceedings of the 27th Lunar and Planetary Science Conference, **1996**.

[13] De la Fuente Marcos, C., de la Fuente Marcos, R. Asteroid (469219) 2016 HO3, the smallest and closest Earth quasi-satellite. *Monthly Notices of the Royal Astronomical Society*, **2016**, 462(4): 3441–3456.

[14] Heiligers, J., Fernandez, J. M., Stohlman, O. R., Wilkie, W. K. Trajectory design for a solar-sail mission to asteroid 2016 HO_3. *Astrodynamics*, **2019**, 3(3): 231–246.

[15] Hu, W. D., Scheeres, D. J. Periodic orbits in rotating second degree and order gravity fields. *Chinese Journal of Astronomy and Astrophysics*, **2008**, 8(1): 108–118.

[16] Yu, Y., Baoyin, H. X. Resonant orbits in the vicinity of asteroid 216 Kleopatra. *Astrophysics and Space Science*, **2013**, 343(1): 75–82.

[17] Wang, X. Y., Jiang, Y., Gong, S. P. Analysis of the potential field and equilibrium points of irregular-shaped minor celestial bodies. *Astrophysics and Space Science*, **2014**, 353(1): 105–121.

[18] Li, X. Y., Qiao, D., Cui, P. Y. The equilibria and periodic orbits around a dumbbell-shaped body. *Astrophysics and Space Science*, **2013**, 348(2): 417–426.

[19] Scheeres, D. J. Dynamics about uniformly rotating triaxial ellipsoids: Applications to asteroids. *Icarus*, **1994**, 110(2): 225–238.

[20] Jiang, Y., Schmidt, J. A., Li, H., Liu, X. D., Yang, Y. Stable periodic orbits for spacecraft around minor celestial bodies. *Astrodynamics*, **2018**, 2(1): 69–86.

[21] Broschart, S. B., Scheeres, D. J., Villac, B. F. New families of multi-revolution terminator orbits near small bodies. In: Proceedings of the AAS/AIAA Astrodynamics Specialist Conference, **2009**.

[22] Scheeres, D. J. Orbit mechanics about asteroids and comets. *Journal of Guidance, Control, and Dynamics*, **2012**, 35(3): 987–997.

[23] Xin, X. S., Scheeres, D. J., Hou, X. Y. Forced periodic motions by solar radiation pressure around uniformly rotating asteroids. *Celestial Mechanics and Dynamical Astronomy*, **2016**, 126(4): 405–432.

[24] Jiang, Y. Equilibrium points and orbits around asteroid with the full gravitational potential caused by the 3D irregular shape. *Astrodynamics*, **2018**, 2(4): 361–373.

[25] Russell, R. P., Lantukh, D., Broschart, S. B. Heliotropic orbits with zonal gravity and shadow perturbations: Application at Bennu. *Journal of Guidance, Control, and Dynamics*, **2016**, 39(9): 1925–1933.

[26] Li, X. Y., Qiao, D., Li, P. Frozen orbit design and maintenance with an application to small body exploration. *Aerospace Science and Technology*, **2019**, 92: 170–180.

[27] Guibout, V., Scheeres, D. J. Stability of surface motion on a rotating ellipsoid. *Celestial Mechanics and Dynamical Astronomy*, **2003**, 87(3): 263–290.

[28] Bellerose, J., Scheeres, D. Dynamics and control for surface exploration of small bodies. In: Proceedings of the AIAA/AAS Astrodynamics Specialist Conference and Exhibit, Honolulu, Hawaii, USA, **2008**: AIAA 2008-6251.

[29] Yu, Y., Baoyin, H. X. Modeling of migrating grains on asteroid's surface. *Astrophysics and Space Science*, **2015**, 355(1): 43–56.

[30] Van wal, S., Reid, R. G., Scheeres, D. J. Simulation of nonspherical asteroid landers: Contact modeling and shape effects on bouncing. *Journal of Spacecraft and Rockets*, **2019**, 57(1): 109–130.

[31] Wen, T. G., Zeng, X. Y., Circi, C., Gao, Y. Hop reachable domain on irregularly shaped asteroids. *Journal of Guidance, Control, and Dynamics*, **2020**, 43(7): 1269–1283.

[32] Li, Z. W., Zeng, X. Y., Wang, S. Q. Hopping trajectory planning for asteroid surface exploration accounting for terrain roughness. *Transactions of the Japan Society for Aeronautical and Space Sciences*, **2021**, 64(4): 205–214.

[33] Scheeres, D. J., Hesar, S. G., Tardivel, S., Hirabayashi, M., Farnocchia, D., McMahon, J. W., Chesley, S. R., Barnouin, O., Binzel, R. P., Bottke, W. F., *et al.* The geophysical environment of Bennu. *Icarus*, **2016**, 276: 116–140.

[34] Li, X. Y., Scheeres, D. J. The shape and surface environment of 2016 HO3. *Icarus*, **2021**, 357: 114249.

[35] Reddy, V., Kuhn, O., Thirouin, A., Conrad, A., Malhotra, R., Sanchez, J. A., Veillet, C. Ground-based characterization of earth quasi satellite (469219) 2016 HO3. In: Proceedings of the 49th AAS/Division for Planetary Sciences Meeting, Provo, Utah, USA, **2017**.

[36] Fohring, D., Reddy, V., Wainscoat, R., Conrad, A., Sharkey, B. Photometry and spectroscopy of (469129) 2016 HO3. In: Proceedings of the 50th AAS/Division for Planetary Sciences Meeting, Knoxville, Tennessee, USA, **2018**.

[37] Ostro, S. J., Pravec, P., Benner, L. A. M., Hudson, R. S., Šarounová, L., Hicks, M. D., Rabinowitz, D. L., Scotti, J. V., Tholen, D. J., Wolf, M., *et al.* Radar and optical observations of asteroid 1998 KY26. *Science*, **1999**, 285(5427): 557–559.

[38] Carry, B. Density of asteroids. *Planetary and Space Science*, **2012**, 73(1): 98–118.

[39] Turcotte, D. L., Schubert, G. *Geodynamics*. Cambridge: Cambridge University Press, **2002**.

[40] Van wal, S. High-fidelity simulation of small-body lander/rover spacecraft. Ph.D. Thesis. USA: University of Colorado, **2018**.

[41] Scheeres, D. J., Ostro, S. J., Hudson, R. S., DeJong, E. M., Suzuki, S. Dynamics of orbits close to asteroid 4179 Toutatis. *Icarus*, **1998**, 132(1): 53–79.

[42] Gómez, G., Masdemont, J. J., Mondelo, J. M. Dynamical substitutes of the libration points for simplified solar system models. In: *Libration Point Orbits and Applications*. Gómez, G., Lo, M. W., Masdemont, J. J. Eds. Word Scientific Publishing Co. Pte. Ltd., **2003**: 373–397.

[43] Broschart, S. B., Lantoine, G., Grebow, D. J. Quasi-terminator orbits near primitive bodies. *Celestial Mechanics and Dynamical Astronomy*, **2014**, 120(2): 195–215.

[44] Montenbruck, O., Gill, E., Lutze, F. H. Satellite orbits: Models, methods, and applications. *Applied Mechanics Reviews*, **2002**, 55(2): B27–B28.

[45] Broucke, R. Stability of periodic orbits in the elliptic, restricted three-body problem. *AIAA Journal*, **1969**, 7(6): 1003–1009.

[46] Grebow, D. Generating periodic orbits in the circular restricted three-body problem with applications to lunar south pole coverage. M.S. Thesis. West Lafayette, Indiana, USA: School of Aeronautics and Astronautics, Purdue University, **2006**.

Xiangyu Li is an associate professor in the School of Aerospace Engineering at Beijing Institute of Technology, China. He was a visiting scholar of University of Colorado at Boulder, USA, in 2019 and 2020. He mainly engages in the research of orbit dynamics in the vicinity of small bodies. E-mail: lixiangy@bit.edu.cn.

Daniel J. Scheeres is a Distinguished Professor in Ann and H. J. Smead Aerospace Engineering Department, University of Colorado Boulder, USA. He mainly engages in the research of celestial mechanics, astrophysics, and space science. E-mail: scheeres@colorado.edu.

Dong Qiao is a professor of aerospace engineering at Beijing Institute of Technology, China. He was selected into the Chang Jiang Scholars Program in 2016 and was a senior visiting scholar in the Department of Mechanical & Aerospace Engineering, University of Strathclyde, UK, in 2013 and 2014. His current research interests include spacecraft dynamics, autonomous control and state estimation, and astrodynamics. E-mail: qiaodong@bit.edu.cn.

Zixuan Liu is a graduate student in Beijing Institute of Technology, China. Her major is the orbital dynamics and state estimation in asteroid exploration.